AQPMC
Association québécoise des physicien(ne)s médicaux cliniques

CONGRÈS SCIENTIFIQUE ANNUEL

12 au 18 novembre 2025

ASSOCIATION QUÉBÉCOISE DES PHYSICIEN(NE)S MÉDICAUX CLINIQUES

NOS COMMANDITAIRES

SUN NUCLEAR
A MIRION MEDICAL COMPANY

Elekta

varian
A Siemens Healthineers Company

visionrt

ACCURAY

RAD formation

MEDRON MEDICAL SYSTEMS INC.
COMING TOGETHER IN HEALTHCARE

RaySearch Laboratories

DONALDSON MARPHIL
Medical

JOUR 1 :

IMAGERIE MÉDICALE

MERCREDI 12 NOVEMBRE 2025

MODÉRATEUR : Sylvain Deschênes, Gerard Lagmago

HORAIRE		PRÉSENTATEUR	TITRE PRÉSENTATION
11h30	11h35	Ouverture de la session	
11h35	12h05	**Charles-Antoine Collins Fekete** Future Leaders Fellow, **University College London**	Scintillateurs plastiques pour la radiographie à protons et le suivi d'objets en temps réel
12h05	12h30	**Jad Farah** Directeur Commercial visionrt	Optimisation de la précision et réduction du temps de traitement par SGRT
12h30	12h45	**Jorge Campos** Étudiant au doctorat en physique **Université McGill**	Toward Magnetic Resonance Oximetry: Development of Multi-Parametric Mapping in Fat-Water Mixtures
12h45	13h00	**Amiel Beausoleil-Morrison** Étudiante à la maîtrise en physique médicale **Université McGill**	Modeling the magnetic resonance signal for oxymetry by fat-water separated relaxation mapping
13h00	13h15	**Mohsen Beikali Soltani** Étudiant au doctorat **Université de Montréal**	Estimation of proton stopping power from optimized combinations of virtual monoenergetic images generated by dual-energy CT
13h15	13h30		Spectral Virtual Non-Contrast Imaging Assisted by Artificial Intelligence Segmentation

Toward Magnetic Resonance Oximetry: Development of Multi-Parametric Mapping in Fat-Water Mixtures

Authors: Jorge Campos Pazmiño, Amiel Beausoleil-Morrison, Renée-Claude Bider, Véronique Fortier, Evan McNabb, and Ives Levesque

Purpose: To develop and validate two MRI-based acquisition methods to jointly measure the fat- and water-specific longitudinal relaxation rates (R_{1f} and R_{1w}, respectively), the effective transverse relaxation rate (R_2^*) and proton density fat fraction (PDFF), aiming towards tissue oximetry.

Introduction: The detection and quantification of tissue hypoxia is a key focus in cancer research, as hypoxia in solid tumors can reduce the effectiveness of radiation therapy[1,2]. Despite its clinical importance, hypoxia is not routinely assessed due to the invasive or resource-intensive nature of available measurement methods. MR-oximetry offers a promising non-invasive and cost-effective alternative for mapping tissue and blood oxygenation by measuring changes in the relaxation rates R_1 and R_2^*, respectively[3]. The sensitivity of R_1 to dissolved oxygen in tissue with sufficient fat content can be increased by measuring R_{1f}, while R_{1w} can be used in tissue with low fat content[4]. Tissue fat content can be measured through the PDFF.

Methods: Two MR-oximetry approaches were designed for measurement of $R_{1f,}$ R_{1w}, R_2*, and PDFF: 1) multi-echo magnetization-prepared 2-rapid gradient echo (ME-MP2RAGE)[5] and 2) fat-water separated driven equilibrium single pulse observation of T_1 (Fat DESPOT)[4]. We designed the ME-MP2RAGE approach for higher accuracy, but this sequence requires long acquisition times. In contrast, Fat DESPOT was designed with lower accuracy in mind but enables rapid, breath-hold imaging in under 30 seconds.

Both approaches were tested in phantoms and in vivo with 3T MRI systems. We assembled a custom phantom with 7 vials (50 mL centrifuge tubes) placed inside a large cylindrical enclosure (Magphan SMR170, The Phantom Laboratories) filled with deionized distilled water mixed with gadobutrol, a gadolinium-based contrast agent (GBCA; Gadovist 1.0 M, Bayer Healthcare) and sodium chloride (concentration 85 mM). The vials inside the phantom were: 1 vial filled with 3% by weight agar gel prepared by mixing deionized distilled water, agar powder (MilliporeSigma Canada Ltd), and GBCA; 5 vials filled with peanut oil (JVF Canada Inc) and agar emulsions[6]; and 1 vial filled with pure peanut oil. A diagram of the phantom is presented in Figure 1 a). ME-MP2RAGE and Fat DESPOT phantom measurements were compared against each other and, in select cases, against established gold-standard methods: inversion recovery spin echo (IR-SE) for R_1 mapping, and multi-echo gradient echo (MGRE) for R_2* and PDFF mapping. In vivo, both

techniques were used to image the lower leg of healthy volunteers. Finally, Fat DESPOT was used to measure $R_{1f,}$ R_{1w}, R_2*, and PDFF in the abdomen of healthy volunteer while tissue oxygen was modulated via a hyperoxic breathing gas challenge. The volunteer was first scanned while breathing room air. The gas was then switched to 100% O_2, which the volunteer continued to breathe during a 10-minute stabilization period. After the stabilization period, volunteer was scanned once more while breathing 100% O_2. Wilcoxon signed rank tests were used to detect changes in MR-based parameters due to inhalation of 100% O_2.

Results and Discussion: In phantoms, R_{1f}, R_{1w}, R_2^*, and PDFF measured by Fat DESPOT and ME-MP2RAGE agreed within 5%, 4%, 12% and 3%, respectively, with similar standard deviations. Figure 1 b) shows the quantitative maps measured with each technique for phantom experiments. In phantoms, ME-MP2RAGE agreed better with reference IR-SE and MGRE measurements for $R_{1f,}$ R_{1w} and PDFF mapping. Fat DESPOT agreed better with the reference for R_2^* mapping. The larger difference in R_2^* between Fat DESPOT and ME-MP2RAGE is likely due to a difference in echo times between the techniques.

In vivo, measurements in the leg showed noticeable differences in R_{1f} values within high PDFF tissues such as bone marrow, with ME-MP2RAGE yielding values (2.7±0.1 s^{-1}) that were closer to those reported in literature[7] compared to Fat DESPOT (4.5±0.2 s^{-1}). Figure 2 a) shows maps of the lower leg in healthy volunteers. Although Fat DESPOT showed slightly lower precision and overestimated R_{1f}, it remains a practical alternative due to the more time-efficient data acquisition and the use of vendor-provided MRI sequences. The higher speed of Fat DESPOT enabled measurements in the abdomen during a gas challenge, as illustrated in Figure 2 b). In the spleen, the median difference in R_{1w} (0.03 s^{-1}) detected between the breathing gas conditions (room air and 100% O_2) was significant (p<0.001).

Conclusion: ME-MP2RAGE is an accurate and precise approach for MRI multiparametric mapping (relaxation and PDFF). Despite its slightly lower precision and accuracy, Fat DESPOT provides benefits in clinical settings that require standard MRI sequences. Moreover, Fat DESPOT enabled fast imaging and detection in changes in MR-based parameters during a breathing gas challenge.

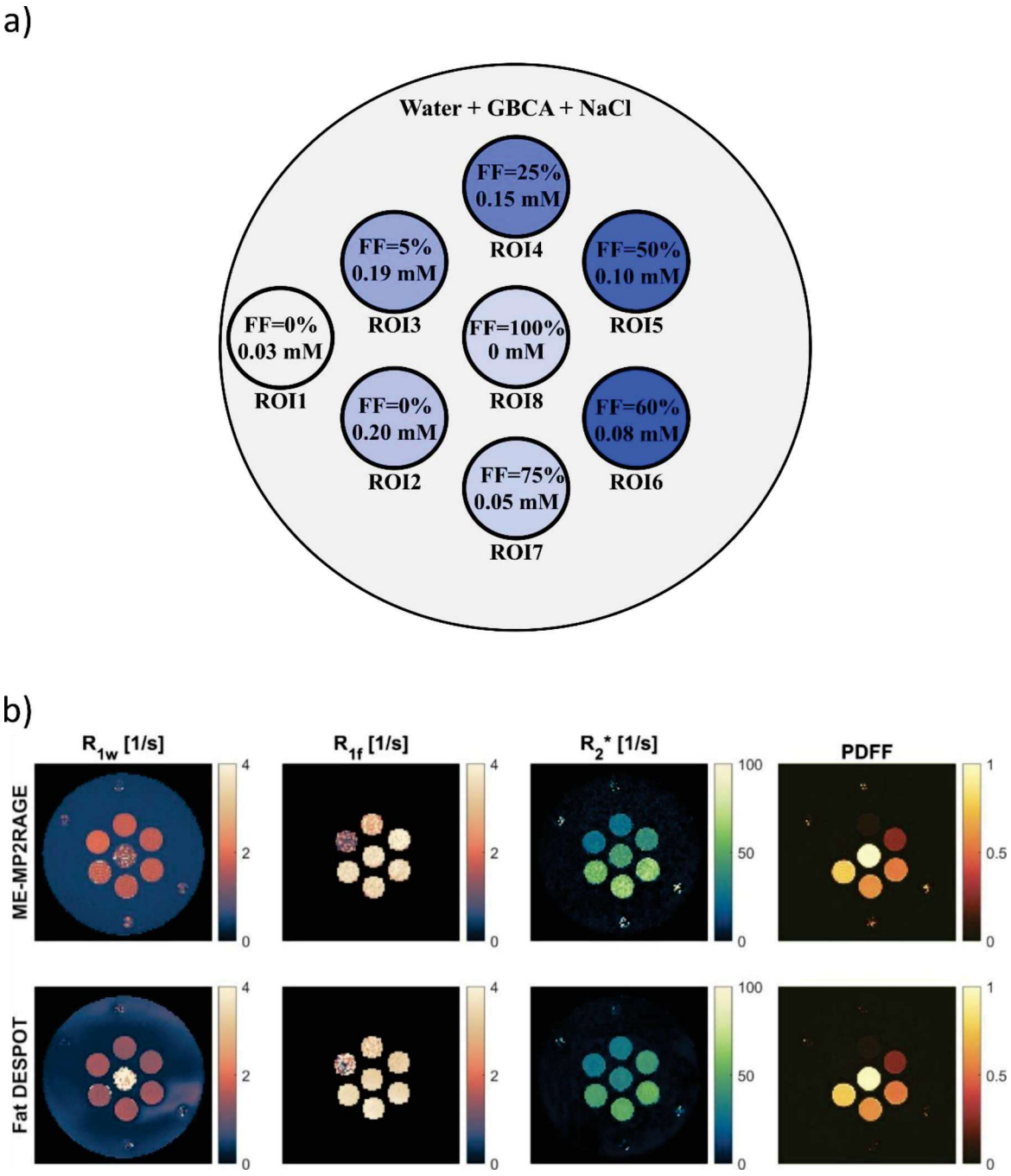

Figure 1: Phantom experiments. a) Phantom diagram with the nominal fat fraction (FF) and GBCA concentration (reported in mM) for each region of interest (ROI) in the phantom. ROI 1 represents the large phantom compartment. ROIs 2-8 represent the vials. b) ME-MP2RAGE (top row) and Fat DESPOT (bottom row) results for phantom experiments. From left to right, quantitative maps are presented for R_{1f}, R_{1w}, R_2^*, and PDFF.

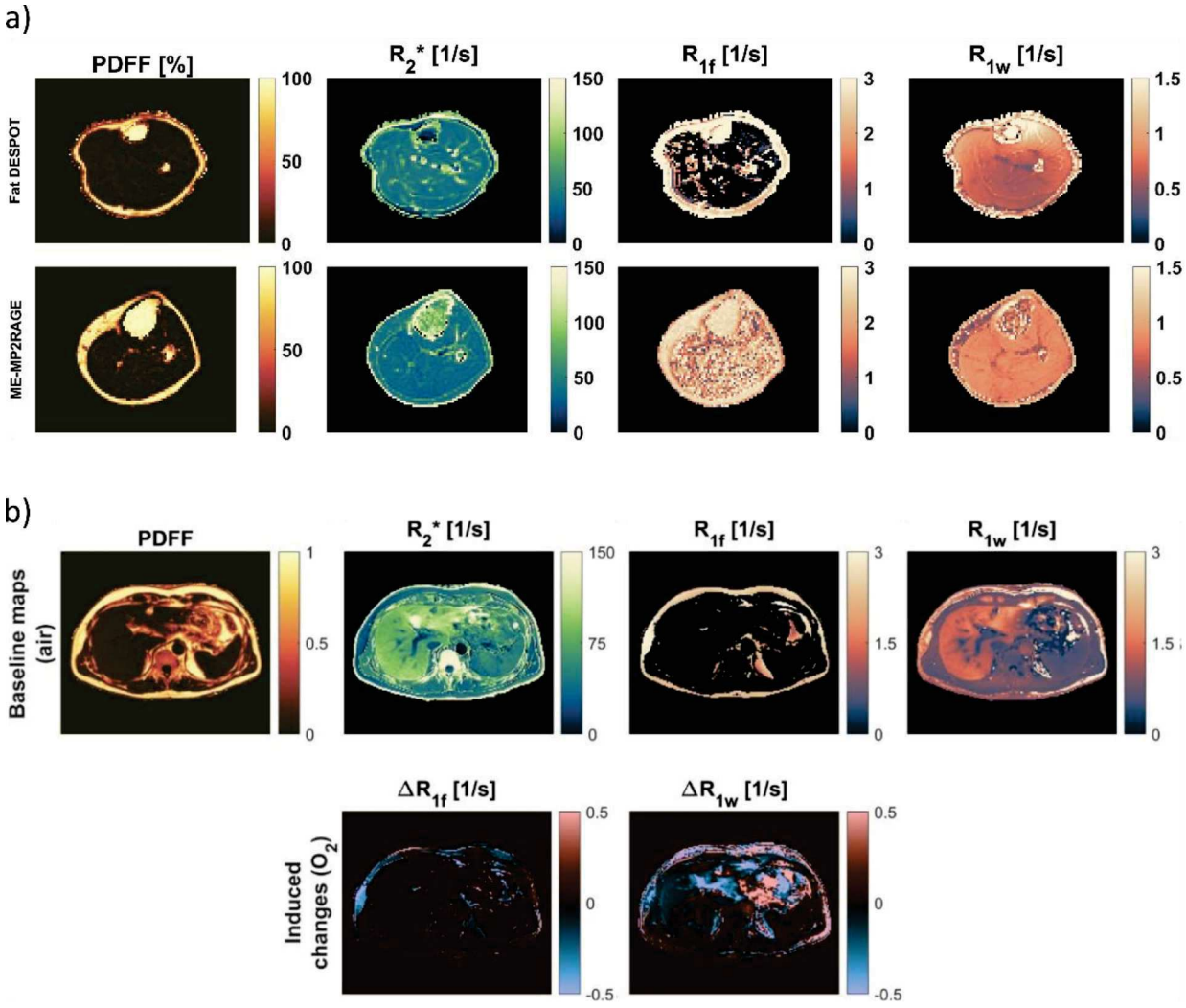

Figure 2: In vivo experiments. a) ME-MP2RAGE (top row) and Fat DESPOT (bottom row) results for in vivo measurements of the lower leg of healthy volunteers. From left to right, quantitative maps are presented for R_{1f}, R_{1w}, R_2^*, and PDFF. b) Fat DESPOT measurement in a hyperoxic breathing gas challenge. Top row presents quantitative maps measured while volunteer breathed room air. Bottom row present changes induced in R_{1f} and R_{1w} due to 100% O_2 inhalation during 10 minutes.

References

1. Hockel M, Vaupel P. Tumor Hypoxia: Definitions and Current Clinical, Biologic, and Molecular Aspects. *JNCI Journal of the National Cancer Institute*. 2001;93(4):266-276. doi:10.1093/jnci/93.4.266

2. Vaupel P, Mayer A. Hypoxia in cancer: significance and impact on clinical outcome. *Cancer Metastasis Rev*. 2007;26(2):225-239. doi:10.1007/s10555-007-9055-1

3. O'Connor JPB, Robinson SP, Waterton JC. Imaging tumour hypoxia with oxygen-enhanced MRI and BOLD MRI. *BJR*. 2019;92(1096):20180642. doi:10.1259/bjr.20180642

4. Fortier V, Levesque IR. MR-oximetry with fat DESPOT. *Magn Reson Imaging*. 2023;97:112-121. doi:10.1016/j.mri.2022.12.023

5. Fortin MA. Fat-water separated T1 mapping with inversion-prepared multi-echo MRI. https://escholarship.mcgill.ca/concern/theses/dv140019h. Accessed December 4, 2023.

6. Bush EC, Gifford A, Coolbaugh CL, Towse TF, Damon BM, Welch EB. Fat-Water Phantoms for Magnetic Resonance Imaging Validation: A Flexible and Scalable Protocol. *J Vis Exp*. 2018;(139):57704. doi:10.3791/57704

7. Bojorquez JZ, Bricq S, Acquitter C, Brunotte F, Walker PM, Lalande A. What are normal relaxation times of tissues at 3 T? *Magnetic Resonance Imaging*. 2017;35:69-80. doi:10.1016/j.mri.2016.08.021

AQPMC abstract – Modelling

Title: Modeling the magnetic resonance signal for oxymetry by fat-water separated relaxation mapping

Authors: Beausoleil-Morrison, Campos, Bider, Fortier, McNabb, Levesque

amiel.beausoleil-morrison@mail.mcgill.ca
jorge.campospazmino@mail.mcgill.ca
renee-claude.bider@mail.mcgill.ca
veronique.fortier@mcgill.ca
evan.mcnabb@muhc.mcgill.ca
ives.levesque@mcgill.ca

Purpose: To develop an accurate signal model for multi-echo, variable flip angle magnetic resonance (MR) mapping of longitudinal and transverse fat-water separated relaxation. This model will be used in data analysis of a fast, precise, and accurate MR-based method for dynamic in vivo tissue oxygenation mapping during a breathing gas challenge.

Introduction: Tumour hypoxia is a marker for disease progression and treatment outcome [1]. It reduces the efficacy of radiation therapy [2], and mapping hypoxia could improve therapy outcomes by enabling dose modulation. Existing approaches to detect tumour hypoxia [3] are too limited for clinical use such that hypoxia is not routinely assessed in patients.

MRI-based oximetry provides a non-invasive and clinically practical alternative for assessing blood and tissue oxygenation by measuring changes in the relaxation rates R_2^* and R_1, respectively[1] (Fat DESPOT) has been proposed by our group to obtain simultaneous measurements of changes in R of fat and water. Previous work with Fat DESPOT in phantoms used the magnitude MRI signal. Using only the magnitude data required longer acquisition times to collect sufficient data for fitting and was inaccurate for the mapping of the proton density fat fraction (PDFF). We hypothesize that (1) modeling the complex signal and (2) explicitly the change in MR parameters expected during the gas challenge will yield more accurate and precise results while reducing data acquisition times.

Methods: First, simulations were used to compare the complex and magnitude fitting approaches using virtual phantom data for fat fractions between 0 and 100%. Using the magnitude Fat DESPOT technique, a 12-echo acquisition was analyzed based on our original protocol [5]. This was compared to an 8-echo simulated acquisition analyzed using the complex approach.

Next, a fat-water emulsion phantom was constructed to compare the magnitude and complex fitting approaches experimentally. The phantom was composed of various mixtures of peanut oil and distilled water-agar solutions doped with a gadolinium-based contrast agent. The phantom

was scanned on a 3 T system. The data was processed using magnitude and complex models. PDFF estimates were compared with a reference measurement in the same phantom.

Finally, the Fat DESPOT model was adapted to jointly fit the complex data from repeated measurements while modelling the changes in relaxation parameters, to capture the change arising from a breathing gas challenge. Cramer Rao Bound (CRB) theory was used to optimize the data acquisition parameters, since this approach maximizes the precision of the parameter estimates. This approach was tested in simulations using a digital MRI phantom of the abdomen and with data from a healthy volunteer. Scans in the healthy individual were acquired under normoxic and hyperoxic breathing gas stimuli. The results of the proposed model were compared to the complex Fat DESPOT approach independently applied to the datasets for the two gasses.

Results and discussion: Fitting the complex data resulted in a smaller relative error and standard deviation when compared to the magnitude approach, shown in Figure 1. This was especially visible in higher fat fractions (60 - 90%). In low fat fractions, using complex fitting decreased the range of R_{1f} values for which Fat DESPOT produces accurate results with a relative error below 20%. The results obtained for the R_{1f} measurements in phantom using complex fitting agreed with previous spectroscopic R_1 measurements [6].

Proton density fat fraction (PDFF) measurements in phantom were accurate with an absolute error below 2% when using the complex fitting approach to Fat DESPOT, while the absolute error on the PDFF measurements using magnitude fitting were larger and inconsistent across fat fractions.

The proposed Fat DESPOT technique tested on the abdomen phantom showed comparable accuracies for baseline R_{1w}, R_{1f}, R_2^*, and PDFF measurements to those obtained using the reference approach (Figure 2). The two techniques were compared using a normalized root mean squared error (nRMSE) for each parameter, with differences of less than 2% between techniques. The proposed joint-fitting approach had higher precision and sensitivity when compared to the reference approach in the healthy volunteer.

Conclusion: The complex approach to the Fat DESPOT technique has been shown to be accurate and precise in measurements of relaxation parameters. This will benefit its use as a method for multi-parametric tissue oxygenation mapping, increasing the potential sensitivity to small changes in blood and/or tissue oxygenation.

References: [1] Vaupel, P., Mayer, A. (2007) Hypoxia in cancer: significance and impact on clinical outcome. Cancer Metastasis Rev., 26(2), 225-239. **[2]** Sørensen, B. S., Horsman M. R. (2020) Tumour hypoxia: Impact on radiation therapy and molecular pathways. Front Oncol., 10, 562. **[3]** Walsh, J.C., Lebedev, A., Aten, E., Madsen, K., Marciano, L., Kolb, H.C. (2014) The clinical importance of assessing tumour hypoxia: relationship of tumour hypoxia to prognosis and therapeutic opportunities. Antioxid. Redox. Signal, 21(10). **[4]** O'Connor, J.P.B., Robinson, S.P., Waterton, J.C. (2019) Imaging tumour hypoxia with oxygen-enhanced MRI and BOLD MRI. Br J Radiol., 92(1095). **[5]** Fortier, V., & Levesque, I. R. (2023). MR-oximetry with fat DESPOT. *Magnetic Resonance Imaging*, *97*, 112-121 **[6]** Fortier, V., & Levesque, I. R. (2022).

Longitudinal relaxation in fat-water mixtures and its dependence on fat content at 3 T. *NMR in Biomedicine*, *35*(2), e4629.

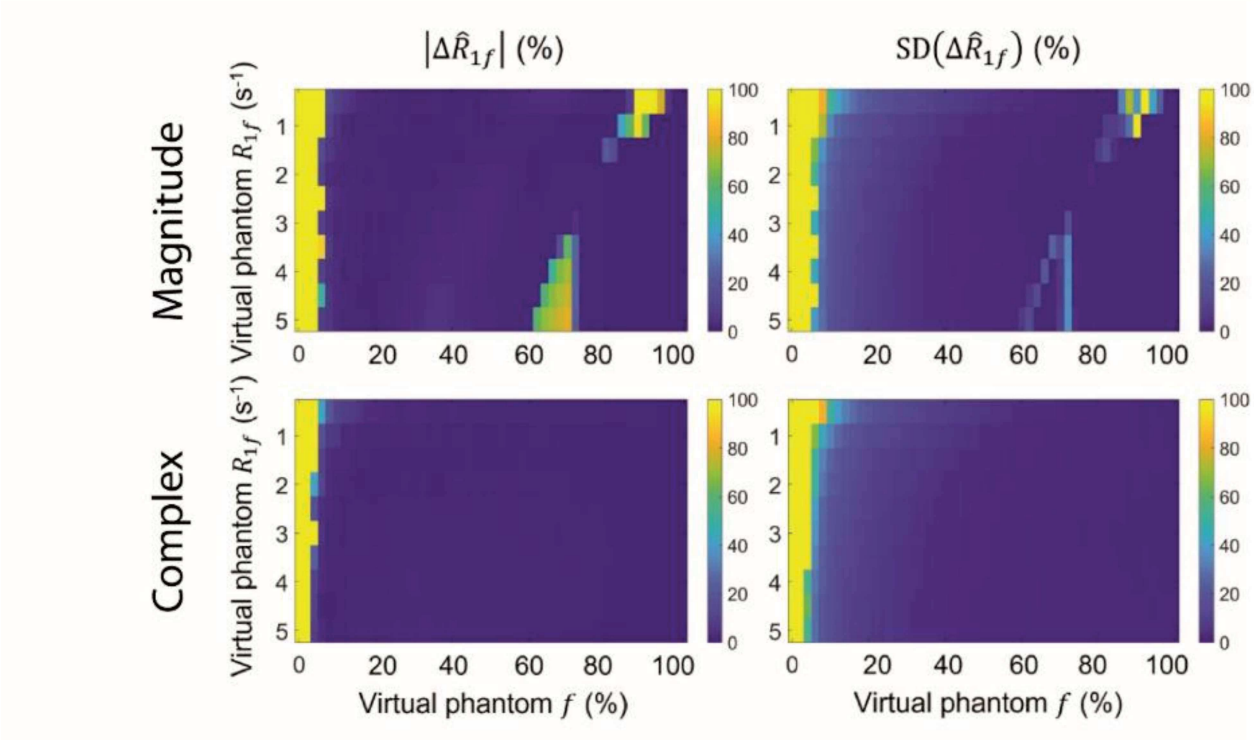

Figure 1: Relative error (left column) and standard deviation (right column) on the R_{1f} estimate for the magnitude (top row) and complex (bottom row) approaches to Fat DESPOT model fitting in simulation. In the magnitude approach, a 12-echo acquisition with TE_1 = 1.5 ms, ΔTE=1.2 ms, TR = 18 ms was simulated. In the complex approach, an 8-echo acquisition with TE_1 = 1.9 ms, ΔTE = 1.8 ms, and TR = 18 ms was simulated.

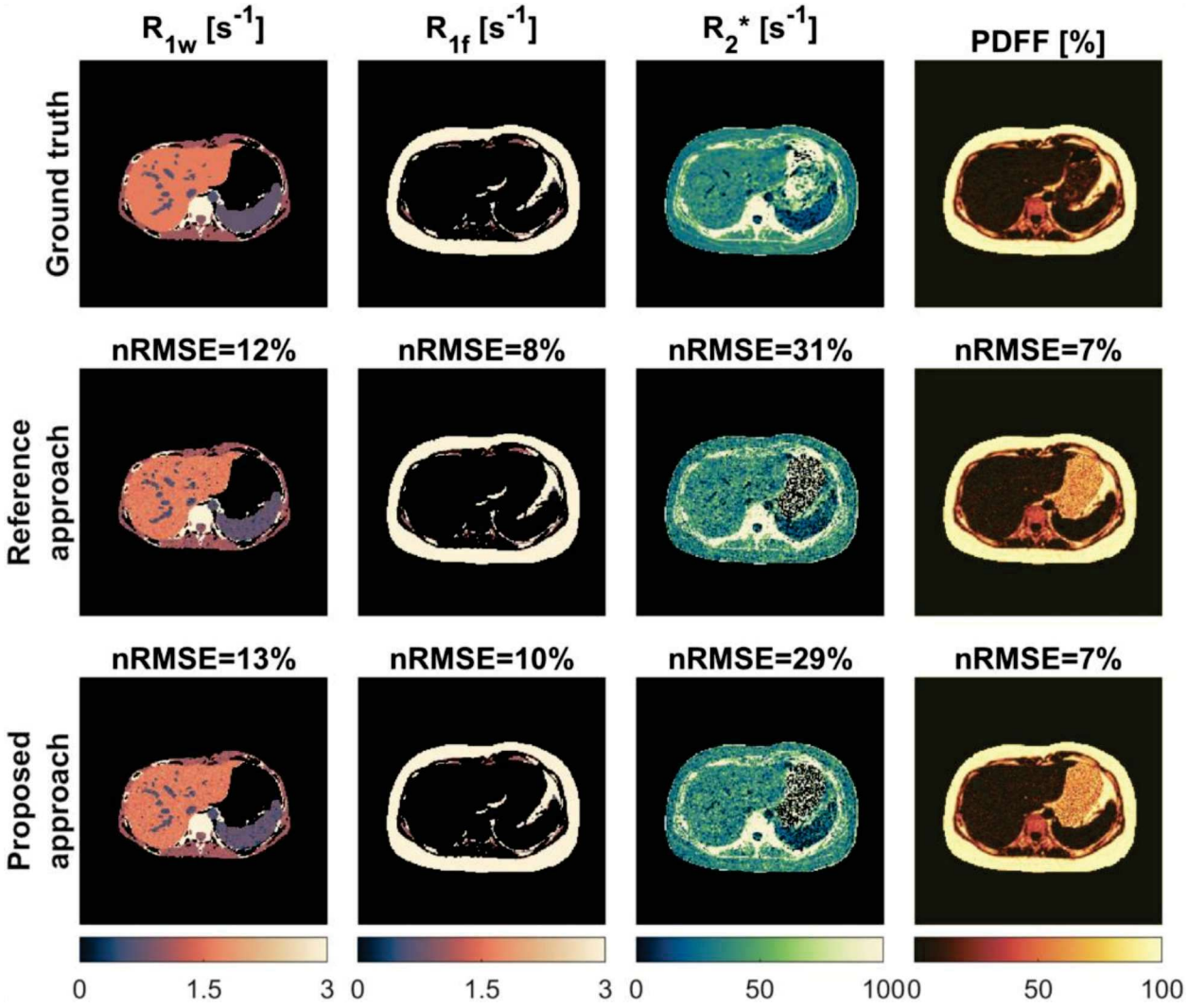

Figure 2: Comparison of the baseline quantitative maps for R_{1w}, R_{1f}, R_2*, and PDFF. Regions of PDFF>50 and PDFF<50 are masked in R_{1w} and R_{1f} maps, respectively. Text above each map reports the nRMSEs calculated when comparing the reference (complex) and the proposed (joint fitting) Fat DESPOT approaches with the corresponding ground truth map. Results are presented for SNR=30.

Estimation of proton stopping power from optimized combinations of virtual monoenergetic images generated by dual-energy CT

Mohsen Beikali Soltani[1,2], Esther Bär[3,4], Edrine Damulira[1,2], and Hugo Bouchard[1,2]

[1] *Département de physique, Université de Montréal, Campus MIL, 1375 Av. Thérèse-Lavoie-Roux, Montréal, QC, Canada, H2V 0B3*

[2] *Centre de recherche du Centre hospitalier de l'Université de Montréal, 900 Rue Saint-Denis, Montréal, QC, Canada, H2X 0A9*

[3] *Department of Medical Physics and Biomedical Engineering, University College London, Gower Street, London WC1E 6BT, United Kingdom*

[4] *University College London Hospitals NHS Foundation Trust, Radiotherapy Physics, 250 Euston Road, London NW1 2PG, United Kingdom*

Introduction

Accurate estimation of proton stopping power ratio (SPR) is crucial for minimizing range uncertainties in proton radiotherapy treatment planning. Conventional single-energy CT (SECT) suffers from intrinsic degeneracy, which can lead to range uncertainties of up to 3 mm. Spectral CT techniques—including dual-energy CT (DECT) and photon-counting CT (PCCT)—offer a promising alternative by enabling improved tissue characterization.

Image-based quantitative spectral CT approaches have traditionally been evaluated on polyenergetic spectral CT images, such as those generated by dual-source DECT systems. Modern scanners, however, do not provide polyenergetic images and instead produce a set of virtual monoenergetic images (VMIs) across a wide energy range. For instance, the Philips Spectral CT 7500 generates 17 VMIs, far exceeding the number of inputs required for image-based DECT quantitative methods. Consequently, an optimal pair of VMIs must be selected to capture the information necessary for accurate tissue characterization.

In the literature, VMIs are often selected at fixed energies (e.g., 50 and 200 keV as proposed by Landry *et al.* [1]), while the additional spectral information contained in the remaining VMIs is neglected. In this work, a data-driven principal component analysis (PCA) strategy is developed to optimally combine the complete VMI set, so that information distributed across all energies is captured and estimation of electron density (ρ_e) and SPR is improved.

Methods

In DECT systems, VMIs are generated from only two independent measurements, leading to strong correlations among them. To reduce redundancy and extract independent information, PCA is applied to derive an optimal pair of components, referred to as eigenimages. A calibration dataset of Hounsfield Unit (HU) values is extracted from 16 VMIs (50–200 keV) of the Gammex-467 phantom. PCA applied to this dataset yielded two eigenimages that captured the majority of spectral variance.

Evaluation is performed in two parts:

1. **Phantom Study:** Thirteen inserts of the Gammex-467 phantom are scanned using a dual-layer DECT system (Spectral CT 7500, Philips Healthcare). The resulting eigenimages are used as input to eigenmaterial decomposition (EMD) [2, 3], to generate ρ_e and SPR maps. Accuracy is assessed against reference values and against scanner provided maps. Figure 1 illustrates the steps for extracting eigenimages and subsequently generating ρ_e and SPR maps

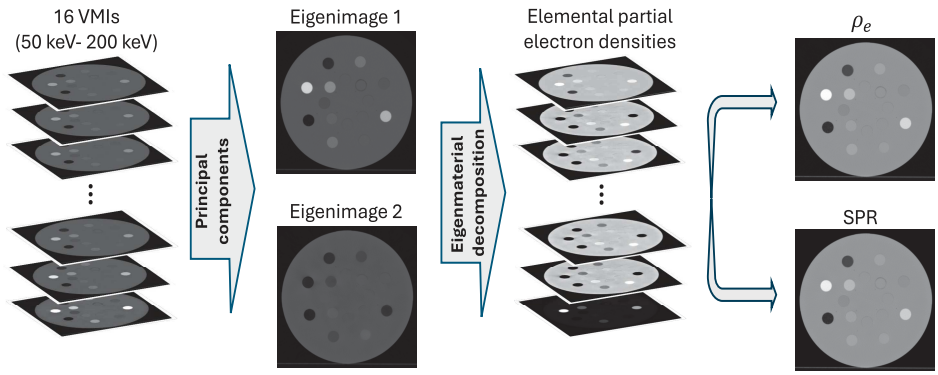

Figure 1: Overview of the proposed method. PCA is applied to 16 VMIs from the Spectral CT 7500 to derive an optimal pair of eigenimages, which are used in EMD to estimate partial electron densities and compute ρ_e and SPR maps.

2. **Simulation Study:** Twelve virtual patient datasets are simulated under non-contrast (NC) and contrast-enhanced (CE) conditions. The PCA-derived eigenimages are used as input to the Bayesian spectral virtual non-contrast (Spectral-VNC) framework, which accounts for tissue variability and noise [4]. Performance is compared to alternative DECT inputs (50/200 keV VMIs, 100/140-Sn kVp polyenergetic images) and to SECT-based conversion methods using 79 keV and 160 keV VMIs.

Results

In the phantom study, the PCA-based method improves accuracy compared to scanner outputs. Across 13 tissue-equivalent inserts, RMS errors in ρ_e decrease from 1.53% to 0.82%, and SPR errors from 1.09% to 0.74%. Mean errors are also reduced, from 1.22% to –0.03% for ρ_e, and from 0.74% to 0.03% for SPR.

In the simulation study, the PCA-derived input consistently yields the lowest RMS errors. For DECT using the Spectral-VNC method, RMS error in the non-contrast setting is 2.56% with eigenimages, compared to 2.98% with 50/200 keV VMIs and 2.72% with polyenergetic images. In the contrast-enhanced setting, eigenimages maintain superior performance with error 2.79% compared to 3.17% and 3.10%, respectively. When used for SECT-based estimation, eigenimage 1 achieves the lowest overall error (RMS 3.03%), outperforming 79 keV (3.52%) and 160 keV (3.96%) VMIs across all tissues. Figure 2 shows the RMS errors in SPR across the six scenarios evaluated in this study

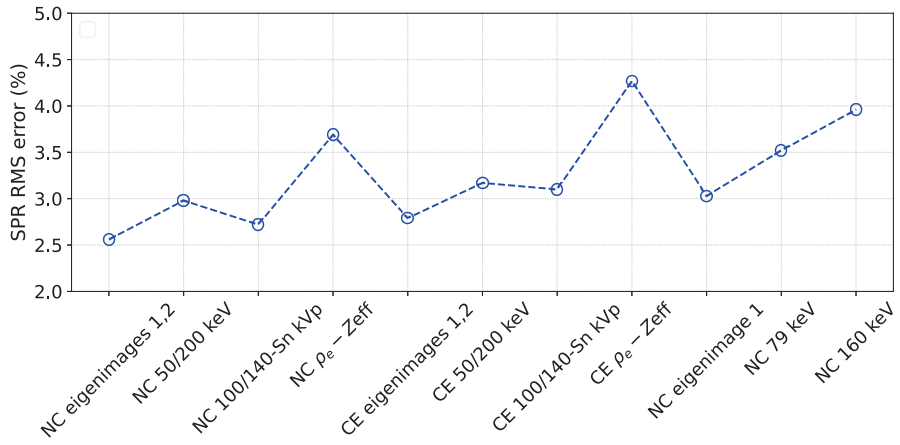

Figure 2: RMS errors in SPR across all simulated patients for the evaluated methods. Dual-energy results are shown for both non-contrast (NC) and contrast-enhanced (CE) data, while the SECT-based method is assessed only on non-contrast images.

Conclusion

The PCA-based VMI selection strategy identifies an optimal image pair, validated on phantom and patient simulations. It improves ρ_e and SPR estimation compared with scanner outputs and alternative VMI choices, demonstrating feasibility and broad applicability for DECT-, PCCT-, and SECT-based proton therapy planning.

Bibliography

[1] G. Landry et al., Relative proton stopping power estimation from virtual monoenergetic images reconstructed from dual-layer Computed Tomography, Medical Physics **46**, 1821–1828 (2019).

[2] A. Lalonde and H. Bouchard, A general method to derive tissue parameters for Monte Carlo dose calculation with multi-energy CT, Physics in medicine & biology **61**, 8044–8069 (2016).

[3] M. Simard, R. K. Panta, S. T. Bell, A. P. Butler, and H. Bouchard, Quantitative imaging performance of MARS spectral photon-counting CT for radiotherapy, Medical Physics **47**, 3423–3434 (2020).

[4] M. Beikali Soltani and H. Bouchard, Dual virtual non-contrast imaging: a Bayesian quantitative approach to determine radiotherapy quantities from contrast-enhanced DECT images, Physics in Medicine & Biology **69**, 245008 (2024).

Spectral Virtual Non-Contrast Imaging Assisted by Artificial Intelligence Segmentation

Mohsen Beikali Soltani[1,2] and Hugo Bouchard[1,2]

[1] *Département de physique, Université de Montréal, Campus MIL, 1375 Av. Thérèse-Lavoie-Roux, Montréal, QC, Canada, H2V 0B3*

[2] *Centre de recherche du Centre hospitalier de l'Université de Montréal, 900 Rue Saint-Denis, Montréal, QC, Canada, H2X 0A9*

Introduction

Accurate tissue characterization is essential in radiotherapy planning, particularly for estimating proton stopping power ratio (SPR) and water-equivalent path length (WEPL), which determine proton beam range. Spectral CT, including dual-energy CT (DECT) and photon-counting CT (PCCT), enables more accurate tissue characterization than conventional single-energy CT (SECT) by providing multiple independent energy measurements per voxel. In contrast-enhanced scans, one degree of freedom is consumed by removing the contribution of contrast agent, which limits tissue characterization. To address this, a dual virtual non-contrast (dual-VNC) method [1] was previously introduced to restore non-contrast HUs from contrast-enhanced DECT data, enabling quantitative approaches such as eigentissue decomposition (ETD) [2].

In this work, dual-VNC is extended by directly integrating ETD into the dual-VNC Bayesian formulation, allowing direct SPR estimation. This unified framework, termed spectral-VNC, generalizes to PCCT with any number of channels. In addition, AI-based whole-body segmentation is integrated as an anatomical prior, which, to the best of our knowledge, is the first integration of pre-trained segmentation models into spectral CT tissue characterization.

Methods

The dual-VNC method estimates non-contrast DECT HUs, $\mathbf{u}_{\mathrm{NC}}$, from contrast-enhanced measurements $\mathbf{u}_{\mathrm{m}}$ by:

$$\left(\hat{\mathbf{u}}_{\mathrm{NC}}, \hat{b}\right) = \underset{\{\mathbf{u}_{\mathrm{NC}}, b\}}{\arg\max} \{p(\mathbf{u}_{\mathrm{m}}|\mathbf{u}_{\mathrm{NC}}, \beta_b), p(\mathbf{u}_{\mathrm{NC}}|b), p(b)\}, \tag{1}$$

where β_b is the relative electron density of the contrast agent and b indexes the 58 reference tissues. Local solutions are computed for each tissue, and the one maximizing the posterior defines $\hat{\mathbf{u}}_{\mathrm{NC}}$.

Here, ETD is integrated directly into the Bayesian framework, yielding eigentissue partial electron densities $\mathbf{y}_{\mathrm{NC}}$:

$$\left(\hat{\mathbf{y}}_{\mathrm{NC}}, \hat{b}\right) = \underset{\{\mathbf{y}_{\mathrm{NC}}, b\}}{\arg\max} \{p(\mathbf{u}_{\mathrm{m}}|\mathbf{y}_{\mathrm{NC}}, \beta_b), p(\mathbf{y}_{\mathrm{NC}}|b), p(b)\}. \tag{2}$$

The extracted $\mathbf{y}_{\mathrm{NC}}$ are then used to estimate elemental partial electron densities and, subsequently, SPR.

This suppresses noise through the likelihood term and accounts for tissue variability via the prior. The formalism extends to PCCT with any number of channels and reduces to the same form for non-contrast scans with $\beta_{\max} = 0$. When the tissue type is unknown, $p(b)$ is uniform (1/58). To improve tissue characterization, anatomical priors from TotalSegmentator, an AI-based whole-body segmentation tool labeling over 100 structures [3], are used to restrict $p(b)$ to relevant tissues, enhancing both accuracy and computational efficiency.

Results

The method is evaluated on eight simulated CT slices under strong contrast-enhanced conditions, with the slices and corresponding TotalSegmentator segmentations shown in Figure 1. Equation 2 is applied to six cases: contrast-enhanced DECT and PCCT with and without segmentation, and non-contrast DECT and PCCT.

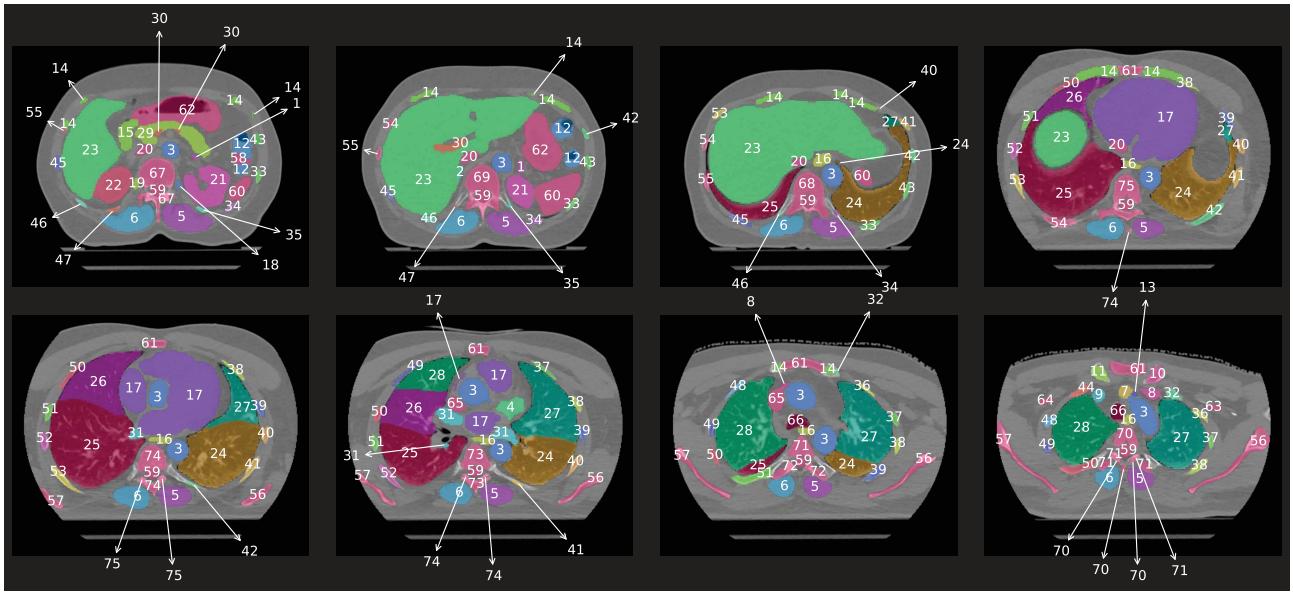

Figure 1: Segmented structures obtained by TotalSegmentator (version v2.4.0) for the eight CT slices used to generate the simulated patients, overlaid on 100 kVp CT images. The segmented structures include: 1,2: Adrenal glands; 3: Aorta; 4: Arterial appendage; 5,6: Autochthon; 7: Brachiocephalic trunk; 8,9: Brachiocephalic arteries; 10,11: Clavicula; 12: Colon; 13: Common carotid artery; 14: Costal cartilage; 15: Duodenum; 16: Esophagus; 17: Heart; 18,19: Iliopsoas; 20: Inferior vena cava; 21,22: Kidneys; 23: Liver; 24-28: Lung lobes; 29: Pancreas; 30: Portal and splenic veins; 31: Pulmonary vein; 32-55: Ribs 1-12; 56,57: Scapulae; 58: Small bowel; 59: Spinal cord; 60: Spleen; 61: Sternum; 62: Stomach; 63,64: Subclavian arteries; 65: Superior vena cava; 66: Trachea; 67-75: Vertebrae (T3-T8, L1, T11, T12).

Integrating segmentation reduced RMS errors in SPR and ρ_e, with larger improvements for PCCT (0.42% and 0.30%) than DECT (0.07% and 0.20%).

To assess the impact on proton-therapy planning, WEPL is computed along 100,000 random beam paths. Figure 2 shows that segmentation consistently reduced WEPL errors, with the strongest effect in PCCT where contrast-enhanced scans with segmentation approached the accuracy of non-contrast scans. For DECT, non-contrast still yielded the smallest WEPL errors, but segmentation substantially narrowed the gap. Importantly, segmentation improved WEPL accuracy more than adding extra energy channels, lowering the median RMS error of contrast-enhanced DECT with segmentation below that of contrast-enhanced PCCT without segmentation.

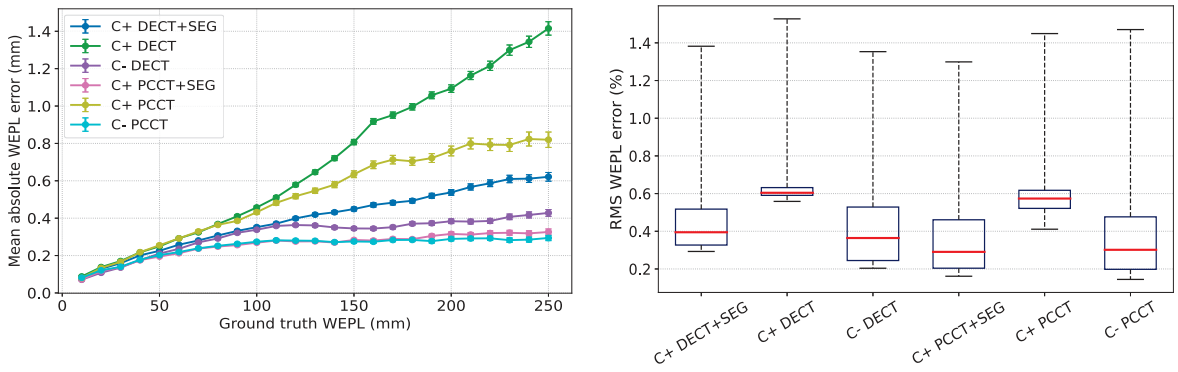

(a) (b)

Figure 2: WEPL errors. (a) Mean absolute errors with 95% confidence intervals. (b) Box-plots of RMS WEPL errors; red lines mark the medians; dashed whiskers span the full range.

Conclusion

This work extends the dual-VNC framework to arbitrary spectral CT channels and incorporates AI-based multi-organ segmentation into the Bayesian optimization. The results demonstrate that segmentation improves SPR and WEPL estimation, with the greatest gains observed for PCCT, indicating the potential of AI to enhance quantitative tissue characterization. Future work will focus on validating the method on clinical contrast-enhanced DECT and PCCT datasets.

Bibliography

[1] M. Beikali Soltani and H. Bouchard, Dual virtual non-contrast imaging: a Bayesian quantitative approach to determine radiotherapy quantities from contrast-enhanced DECT images, Physics in Medicine & Biology **69**, 245008 (2024).

[2] A. Lalonde and H. Bouchard, A general method to derive tissue parameters for Monte Carlo dose calculation with multi-energy CT, Physics in medicine & biology **61**, 8044–8069 (2016).

[3] J. Wasserthal, H.-C. Breit, M. T. Meyer, M. Pradella, D. Hinck, A. W. Sauter, T. Heye, D. T. Boll, J. Cyriac, S. Yang, M. Bach, and M. Segeroth, TotalSegmentator: Robust Segmentation of 104 Anatomic Structures in CT Images, Radiology: Artificial Intelligence **5**, e230024 (2023).